Langmuir

Article

pubs.acs.org/Langmuir

Conversion of Methane to Methanol with a Bent Mono(μ-oxo)dinickel Anchored on the Internal Surfaces of Micropores

Junjun Shan,[†] Weixin Huang,[†] Luan Nguyen,[†] Ying Yu,[‡] Shiran Zhang,[†] Yuanyuan Li,[§] Anatoly I. Frenkel,[§] and Franklin (Feng) Tao*[,†]

[†]Department of Chemistry and Biochemistry, University of Notre Dame, Notre Dame, Indiana 46556, United States

[‡]College of Physical Science and Technology, Central China Normal University, Wuhan 430079, China

[§]Department of Physics, Yeshiva University, New York, New York 10000, United States

Supporting Information

ABSTRACT: The oxidation of methane to methanol is a pathway to utilizing this relatively abundant, inexpensive energy resource. Here we report a new catalyst, bent mono(μ-oxo)dinickel anchored on an internal surface of micropores,which is active for direct oxidation. It is synthesized from the direct loading of a nickel precursor to the internal surface of micropores of ZSM5 following activation in O_2. Ni $2p_{3/2}$ of this bent mono(μ-oxo)dinickel species formed on the internal surface of ZSM5 exhibits a unique photoemission feature, which distinguishes the mono(μ-oxo)dinickel from NiO nanoparticles. The formation of the mono(μ-oxo)dinickel species was confirmed with X-ray absorption near-edge structure (XANES) and extended X-ray absorption fine structure (EXAFS). This mono(μ-oxo)dinickel species is active for the direct oxidation of methane to methanol under the mild condition of a temperature as low as 150 °C in CH_4 at 1 bar. In-situ studies using UV−vis, XANES, and EXAFS suggest that this bent mono(μ-oxo)dinickel species is the active site for the direct oxidation of methane to methanol. The energy barrier of this direct oxidation of methane is 83.2 kJ/mol.

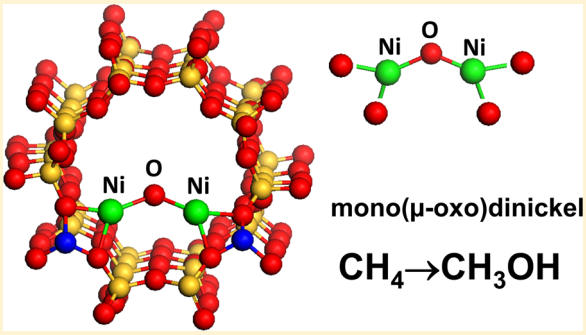

1. INTRODUCTION

CH_4 is a relatively inexpensive, abundant resource compared to others. CH_3OH is one of the most important raw materials in the chemical industry for the production of numerous commodities. In addition, it is an energy carrier providing energy for portable devices through low-temperature fuel cell technology. Interest in the utilization of methanol has largely increased in the recent decade due to the potential for the commercialization of low-temperature methanol fuel cell technology. Currently, the production of CH_3OH from CH_4 in the chemical industry is a two-step process. The first step is the conversion of methane to synthesis gas (CO and H_2) by steam reforming of methane; the second step is the synthesis of methanol from CO and H_2.[1−3] Unfortunately, the first step is performed at a rather high temperature of 600−800 °C, which significantly increases the energy consumption and the cost of the industrial footprint. To economically utilize CH_4 to produce CH_3OH, a process to synthesize CH_3OH from CH_4 under mild conditions is needed.

From a thermodynamic point of view, the synthesis of CH_3OH directly from CH_4 is energetically favorable even at room temperature at the ambient pressure of CH_4. However, it is known that the activation of the C−H bond of CH_4 is the most challenging elemental step due to the strong C−H bond (436 kJ/mol). In addition, controllably partial oxidation of CH_4 to a specific fuel molecule, methanol, is another challenge since the complete oxidation of CH_4 to CO_2 and H_2O readily happens[4,5] in contrast to partial oxidation. Thus, the prevention of the complete oxidation of CH_4 remains quite challenging in the partial oxidation of methane to methanol.

Nature partially oxidizes methane to methanol. For instance, methane monooxygenases (MMO), an enzyme in nature, directly converts methane to methanol at ambient temperature.[6−13] The active sites in MMO could be bis(μ-oxo)di-iron complexes or bis(μ-oxo)dicopper complexes as shown in Scheme 1 or even another bridge oxide structure. Scientists have expended significant effort to mimic the catalysis of MMO by developing artificial catalysts that have similar active sites.[14−24]

Here we synthesized Ni-ZSM5 catalysts consisting of bent mono(μ-oxo)dinickel species on the internal wall of ZSM5 by impregnation of the Ni precursor and then activation in O_2. Catalytic measurements show that this Ni-ZSM5 is active for the conversion of CH_4 to CH_3OH. In-situ characterization using multiple techniques shows that the active sites are bent mono(μ-oxo)dinickel in ZSM5.

Received: April 1, 2014
Revised: May 18, 2014
Published: June 4, 2014

Scheme 1. Schematic of the Bis(μ-oxo)dimetal Structure in MMO Active for Methane Conversion to Methanol

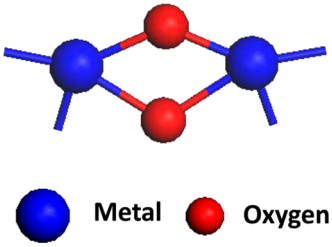

2. EXPERIMENTAL SECTION

The Ni-ZSM5 catalysts were synthesized through two steps. The first step is the preparation of H-ZSM from zeolite NH_4-ZSM5 with a Si/Al ratio of 15 (Alfa) by calcination in air at 400 °C for 12 h.[25] The inductively coupled plasma (ICP) measurements showed that the concentrations of Cu and Fe in the purchased NH_4-ZSM5 are 0 and 0.0019 wt %, respectively. Such low concentrations of Cu and Fe impurities will not produce detectable product. The second step is the introduction of Ni cation into the internal wall of ZSM5 through impregnating 30 mL of a nickel nitrate solution (99%, Sigma-Aldrich) at 65 °C with continuous stirring (450 rpm) in a gram of H-ZSM5. Filtration upon impregnation was included in the synthesis of some of the catalysts studied in this work. In the filtration step, the products upon impregnation were washed with distilled water for several cycles. For these catalysts synthesized through filtration, they are termed Ni-ZSM5 with filtration. For catalysts prepared without filtration, they are called Ni-ZSM5 without filtration. After impregnation, the products were dried in a vacuum oven at 60 °C for overnight and calcinated in air at 550 °C for 3 h. Ni-ZSM5 catalysts with different nominal loadings of nickel precursor were synthesized. The concentrations of Ni in Ni-ZSM5 were determined with ICP optical emission spectrometry (ICP-OES). After synthesis, Ni-ZSM5 catalysts were characterized with X-ray diffraction (XRD), transmission electron microscopy (TEM), X-ray absorption near-edge structure (XANES), extended X-ray absorption fine structure (EXAFS), ultraviolet−visible spectroscopy (UV−vis), and X-ray photoelectron spectroscopy (XPS).

XRD patterns of Ni-ZSM5 were collected on a Bruker D8 advance XRD using nickel-filtered Cu Kα radiation (λ = 1.54056 Å). The measurements were operated at 40 kV and 40 mA in continuous mode with a scanning rate of 4.2° min^{-1}. TEM (FEI, Titan 80-300) was operated at an acceleration voltage of 200 kV. Image analysis was done with Digital Micrograph (Gatan) software. The samples for TEM characterization were prepared by dropping their colloidal solutions onto copper grids supported on carbon films.[26−30]

To avoid direct exposure of the catalyst to the ambient environment upon activation or catalysis, a high-pressure reaction cell was attached to a vacuum XPS system. The high-pressure reaction cell has the capability of performing catalysis in a mixture of reactants up to 20 bar while a sample is at a temperature of up to 600 °C°. This reaction cell was designed to experimentally simulate a fixed-bed flow reactor. Flow rates of reactants were measured with flow meters capable of measuring a flow rate at a pressure up to 20 bar. After a reaction performed at a certain temperature in the flowing mixture of reactants at a certain pressure, all reactant gases were purged and the cell was opened to the vacuum environment of the chamber. Then, the catalyst was transferred to the XPS chamber in the UHV environment. This system allows us to track the surface chemistry of a catalyst after activation or catalysis without any exposure of the reacted catalyst to air. Therefore, the surface chemistry of a Ni-ZSM5 catalyst after activation in O_2 or/and a catalysis with CH_4 can be studied with XPS before they are exposed to ambient conditions. In addition, the XPS system is equipped with an argon ion sputter gun to sputter the sample for the depth-profile analysis of chemistry at different depths below the sample surface.

Ni-ZSM5 catalyst (100 mg) was loaded into a fixed-bed flow reactor. For the activation of the catalyst with oxygen, pure O_2 or 5% O_2 (balanced in Ar) at a specific temperature in the range of 450−700 °C was introduced and kept for flowing at a flow rate of 20 mL/min for 3 h. After this activation, the catalyst was cooled to room temperature under O_2 flow. Reaction in terms of the direct conversion of methane to methanol was performed by introducing CH_4 (10% balanced in Ar) at a flow rate of 20 mL/min at room temperature. Catalysis was performed in the temperature range of 125−300 °C for 45 min. Then, the catalyst was cooled to room temperature in CH_4. After the reaction, the methanol molecules formed during this catalysis were extracted with H_2O through a hydrolysis process. The reacted Ni-ZSM5 catalyst was quickly poured into a vial containing 1.0 mL of deionized H_2O. The vial was vigorously stirred at room temperature for 24 h and subsequently centrifuged for 5 min to separate the solvent from Ni-ZSM5 particles. During steps of extraction and centrifugation, the vial was tightly sealed to prevent pollution from the foreign environment. Then, the supernatant was collected for analysis with NMR. The amounts of products were quantified with NMR. ^{1}H NMR spectra were measured on a Bruker AVANCE III HD 400 spectrometer. The measurement was calibrated by using the 3-(trimethylsilyl)-1-propanesulfonic acid sodium salt (DSS) residual signal at δ = 0.0 ppm. Usually, 0.7 mL supernatant was mixed with 0.1 mL of D_2O (with 0.01 wt % DSS) to make a solution in an NMR sample tube for NMR measurements. The concentration of protons in the solvent was much higher than that of products in solution. All ^{1}H NMR spectra were therefore measured using a presaturation solvent suppression technique to suppress the strong H_2O signal.[31] A typical ^{1}H NMR spectrum is provided in Figure S2. The identified products in Figure S2 were methanol (δ = 3.35 ppm), ethylene glycol (δ = 3.66 ppm), and formic acid (δ = 8.44 ppm). These products were quantified in NMR by calibration against authentic standards. (The detailed procedures are present in Supporting Information, Figure S3). This is a qualitative analysis of products from the direct conversion of methane through the above partial oxidation.

In order to determine the concentrations of the obtained products quantitatively, initially the standard curve was obtained by measuring a series of samples with a certain known concentration of a specific product. $A_{\text{standard solution}}/A_{\text{DSS}}$, the ratio of the area of the standard/area of DSS in these samples, was plotted as a function of the concentration of these standard solutions. With this method, the standard curve of methanol was made, as shown in Figure S3. A slope was obtained from this curve. The concentration of an identified product in a sample was determined by dividing the ratio $A_{\text{unknown sample}}/A_{\text{area of DSS}}$ by the slope of the standard curve in the same water/D_2O solvent mixture. With the same method, the concentrations of other products were measured.

In-situ X-ray absorption spectroscopy measurements of catalysts during catalysis were performed at the National Synchrotron Light Source, Brookhaven National Laboratory. The Ni K-edge measurements were performed at the X18B beamline in transmission mode using ionization chamber detectors. The samples were made by pressing the powders into circular pellets using a hydraulic press and transferred them onto a c-shaped sample holder of a Nashner-Adler in-situ cell.[32] The samples were heated through conduction from a heating cartridge outside of the cell. Reactant gases of O_2 and CH_4 were mixed with pure He to make a gas mixture with the same composition as that used in the catalysis measurements.

The data in the XANES region of the absorption coefficient were examined by applying the same procedure for pre-edge line fitting, postedge curve fitting, and edge-step normalization to all data. EXAFS data analysis was performed with the IFEFFIT package and FEFF6 theory. Data modeling at different temperatures was performed using standard procedures.[33,34] Several parameters describing the electronic properties, specifically, the correction to the photoelectron energy origin and the local structural environment (coordination number (N), bond length (R), and mean squared disorder parameter (σ^2)) of the nearest neighbors around absorbing atoms were varied in the fit. More details of the fit are described in the Results and Discussion.

dx.doi.org/10.1021/la501184b | Langmuir 2014, 30, 8558−8569

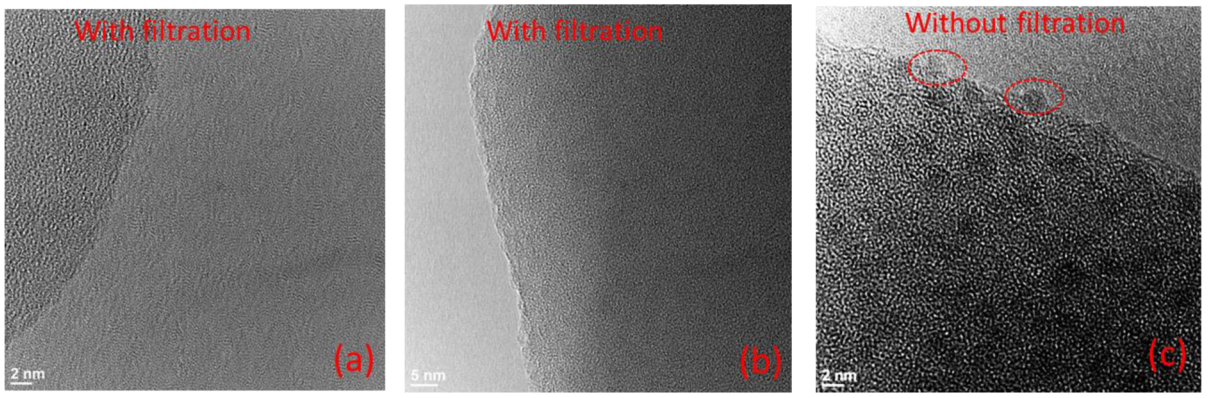

Figure 1. TEM images of 2.5 wt % Ni-ZSM5 catalysts. (a, b) 2.5 wt % Ni-ZSM5 catalyst with filtration. (c) 2.5 wt % Ni-ZSM5 catalyst without filtration.

3. RESULTS AND DISCUSSION

3.1. Synthesis of a Unique Ni-Based Oxide Structure Formed on the Internal Surfaces of Micropores. Figure 1 presents the high-resolution TEM images of 2.5 wt % Ni-ZSM5 with filtration and without filtration. Figure 1c clearly shows that NiO nanoparticles did form on the external surface of a ZSM5 particle of 2.5 wt % Ni-ZSM5 without filtration. They were marked with red circles in Figure 1c, while there is a lack of NiO nanoparticles on the external surface of 2.5 wt % Ni-ZSM5 with filtration (Figure 1a,b).

The XRD patterns of 2.5 wt % Ni-ZSM5 samples are shown in Figure 2. For comparison, XRD patterns of pure NiO nanoparticles[35−37] and pure H-ZSM5[38,39] were collected and are included in Figure 2a,b, respectively. It clearly shows that the XRD of 2.5 wt % Ni-ZSM5 without filtration (Figure 2c) has the (200) diffraction peak of NiO, though the (111) diffraction peak of NiO (marked with a blue arrow) overlapped with peaks of the ZSM5. It also suggests the presence of NiO nanoparticles on the external surface of ZSM5. In the XRD of 2.5 wt % Ni-ZSM5 with filtration (Figure 2e,f) there are no any diffraction patterns attributable to NiO nanoparticles, suggesting that the amount of NiO presented on the external surface of ZSM5 is below the detection limit of XRD. In fact, the XPS studies to be described in this section confirmed that there is no NiO nanocluster formed on the external surface of 2.5 wt % Ni-ZSM5 with filtration. In addition, all XRD patterns of both 2.5 wt % Ni-ZSM5 with filtration and without filtration remain diffraction patterns of pure ZSM5 (Figure 2b), suggesting that the ZSM5 structure remains upon impregnation and the following activation and reaction on Ni-ZSM5 did not modify the structure either.

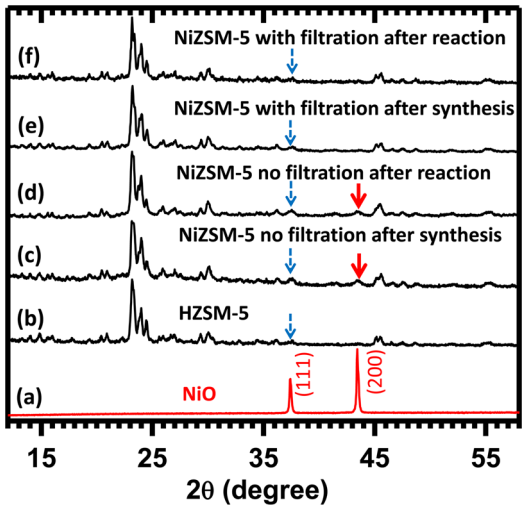

Figure 2. XRD patterns of 2.5 wt % Ni-ZSM5 with and without filtration. For comparison, the XRD patterns of NiO nanoparticles and H-ZSM5 were also included in a and b, respectively.

Figure 3 shows the XPS spectra of 2.5 wt % Ni-ZSM5 with filtration and without filtration. Figure 3a3 shows the photoemission features of Ni $2p_{3/2}$ of pure NiO (Aldrich, 99.0%) collected in our group. As reported in the literature,[40−48] two satellite peaks of Ni $2p_{3/2}$ photoemission at 855.5 and 861.3 eV were observed. Before Ar sputtering, the spectrum of 2.5 wt % Ni-ZSM5 without filtration (Figure 3a2) exhibits photoemission features at 855.5 and 861.3 eV very similar to those of pure NiO (Figure 3a3). They are attributable to satellite peak of Ni $2p_{3/2}$ of NiO nanoparticles on ZSM5 observed in TEM studies (Figure 1c).[40−48] However, the spectrum of 2.5 wt % Ni-ZSM5 with filtration (Figures 3b1) does not show any photoemission feature of Ni $2p_{3/2}$. The difference between Figure 3a2 and 3b1 clearly shows that the filtration is effective in the removal of nickel precursor left on the external surface of ZSM5 particles in the impregnation step. To study the Ni-based species anchored on the internal surface of the micropores of 2.5 wt % Ni-ZSM5 with filtration, we must remove the oxide surface layers of ZSM5 in the catalyst particles. After Ar^+ sputtering of 2.5 wt % Ni-ZSM5 with filtration for 5 min, enough layers of silica on the external surface of 2.5 wt % Ni-ZSM5 with filtration were removed. Thus, the photoemission feature of Ni $2p_{3/2}$ contributed by the Ni-based species anchored on the internal zeolite pores was clearly identified in Figure 3b2. It is noted that there is the main peak of Ni $2p_{3/2}$ at 854.0 eV observed in Figure 3b2. The lack of satellite peaks of Ni $2p_{3/2}$ will be rationalized in the following section. Figure 3c was used schematically to present how we collected photoelectrons generated from the anchored Ni-based species on the internal surfaces of pores of ZSM5 by removing the silica layers of the catalysts and the external NiO nanoparticles, if any. In addition, it is noted that the photoemission feature of Ni $2p_{3/2}$ of the Ni-based species on the internal wall (Figure 3b2−b4) is quite different from that of NiO nanoclusters on the external surface of ZSM5 particles (Figure 3a2).

The 2.5 wt % Ni-ZSM5 samples were characterized by UV−vis spectroscopy. The spectra for 2.5 wt % Ni-ZSM5 without

dx.doi.org/10.1021/la501184b | Langmuir 2014, 30, 8558−8569

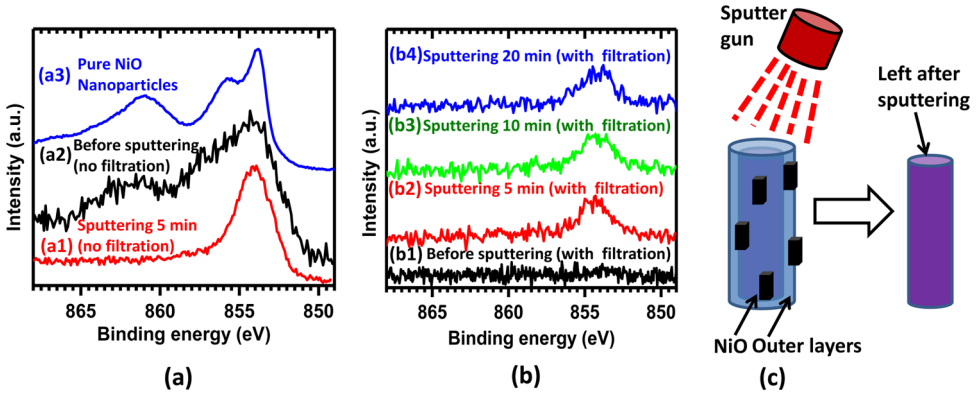

Figure 3. (a) XPS spectra of 2.5 wt % Ni-ZSM5 without filtration before and after sputtering. For comparison, the XPS spectrum of NiO nanoparticles was included in a3 as well. (b) XPS spectra of 2.5 wt % Ni-ZSM5 with filtration before and after sputtering for various amounts of time. (c) Schematic showing how XPS spectra were acquired after removing the outer layers of ZSM5 and the external NiO nanocluster with Ar^+ sputtering.

filtration (Figure 4a,b) have a dominant feature at 33 000 cm^{-1}. This feature is the absorption feature of NiO nanoparticles.[49]

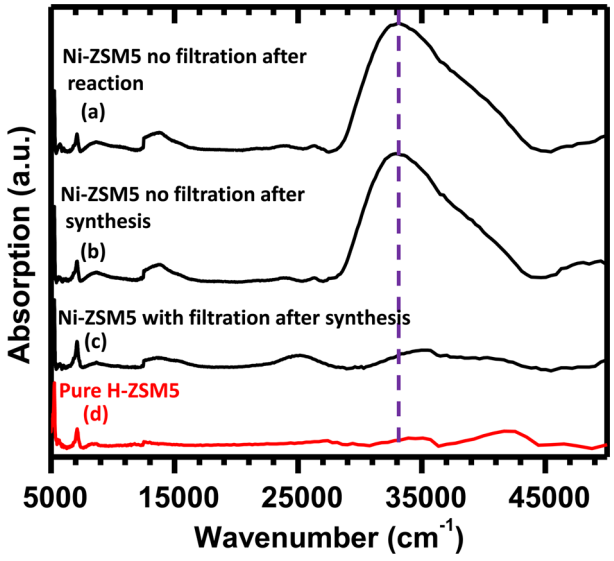

Figure 4. UV−vis spectra of 2.5 wt % Ni-ZSM5 with and without filtration under various conditions. For comparison, the UV−vis spectrum of H-ZSM5 was included in plot d as well.

For 2.5 wt % Ni-ZSM5 with filtration, this feature is negligible (Figure 4c). Thus, UV−vis spectra showed that the amount of NiO left on the external surface of ZSM5 is below the detection limit of UV−vis if the extra precursor of Ni loaded on the external surface of ZSM5 was filtered after the impregnation.

For a catalyst of 2.5 wt % Ni-ZSM5 with filtration, the observed Ni $2p_{3/2}$ signal is contributed by Ni atoms anchored on the internal surface of the pores of the ZSM5 since there is no Ni $2p_{3/2}$ signal for collection before sputtering. The lack of a satellite peak of Ni $2p_{3/2}$ clearly suggests that there are no NiO nanoclusters formed on 2.5 wt % Ni-ZSM5 with filtration. To study the chemistry in the micropores of the catalyst, sputtering is necessary. An immediate question is how many surface layers of the 2.5 wt % Ni-ZSM5 with filtration should be removed before Ni $2p_{3/2}$ can be collected to evaluate the atomic ratio of Ni/Al. In fact, after 5 min of sputtering there is no further change in the photoemission intensity of Ni $2p_{3/2}$ (Figure 3b2−b4) and Al 2p. The possible reasons for the lack of a thickness-dependent distribution of Ni species are discussed in the Supporting Information, section S1. The constant photoemission intensity regardless of the number of layers of silica removed before XPS studies made the calculation of the Ni/Al atomic ratio straightforward. Thus, it is not necessary to consider the layers of silica to be removed in the measurements of the ratios of Ni loaded on the internal wall of ZSM5 to Al atoms in ZSM5.

In terms of sample 2.5 wt % Ni-ZSM5 without filtration, it was sputtered to make sure that the NiO left on the external surface of the catalyst particles was completely removed by sputtering. A complete removal of the NiO nanoparticles on the external surface of the catalyst particles was confirmed by the disappearance of the satellite photoemission feature of Ni $2p_{3/2}$ of NiO at 861.0 and 856.0 eV. This is because that the photoemission feature of Ni $2p_{3/2}$ of NiO nanoparticles is different from that of Ni-based oxide species formed on the internal surface of micropores; the difference is the lack of satellite peaks at 861.0 and 856.0 eV of Ni $2p_{3/2}$ for the specific Ni-based oxide species formed on the micropores. The

Table 1. Overall Atomic Ratio of Ni to Al Based on ICP and XPS Measurements and the Estimated Atomic Ratio of All Ni Atoms to All Al Atoms on the Internal Surface of the Micropores of the Catalysts

sample	overall Ni/Al atomic ratio in Ni-ZSM5 based on ICP measurement	overall Ni/Al atomic ratio in Ni-ZSM5 based on XPS measurement	estimated atomic ratio of all Ni to all Al on the internal surface of micropores in Ni-ZSM5
2 wt % Ni-ZSM5 with filtration	0.05	0.05	0.13
5 wt % Ni-ZSM5 with filtration	0.10	0.12	0.32
10 wt % Ni-ZSM5 with filtration	0.17	0.18	0.48

dx.doi.org/10.1021/la501184b | *Langmuir* 2014, 30, 8558−8569

similarity of the two types of Ni cations is the main peak of Ni 2p at 853.8 eV, which is the main photoemission feature of Ni^{2+}. Their similarity and difference will be further discussed in the next subsection. After a 5 min sputtering of 2.5 wt % Ni-ZSM5 without filtration, a single peak at 854.0 eV of Ni^{2+} appeared (Figure 3a1). The identity of the photoemission feature of Ni $2p_{3/2}$ of 2.5 wt % Ni-ZSM5 without filtration after sputtering (Figure 3a1) and that of 2.5 wt % Ni-ZSM5 with filtration after sputtering (Figure 3b2) clearly suggested that Ni formed the same Ni-based oxide species on the internal wall of ZSM5. The better signal-to-noise ratio of Ni $2p_{3/2}$ of 2.5 wt % Ni-ZSM5 without filtration but with sputtering (Figure 3a1) in contrast to Ni 2p3/2 of 2.5 wt % Ni-ZSM5 with filtration (Figure 3b2) results from the actual larger loading in 2.5 wt % Ni-ZSM5 without filtration, which will be discussed in section 3.3. The bulk atomic ratio of Ni to Al in terms of the overall atomic ratio of Ni to Al of the whole catalyst was measured with ICP (Table 1). For the calculation of Ni/Al atomic ratios of 5 wt % Ni-ZSM5 with filtration and 10 wt % Ni-ZSM5 with filtration with XPS, both Ni $2p_{3/2}$ and Al 2p XPS spectra were collected after sputtering the catalyst to remove silica layers. The Ni $2p_{3/2}$ spectra collected from the two samples after a sputtering of 10 min have only the main peaks of Ni $2p_{3/2}$ of Ni^{2+}. There are not any satellite peaks.

Table 1 also lists the estimated atomic ratio of all Ni atoms on the internal surfaces of the micropores to all Al atoms on the internal surfaces of the micropores. The ratio was roughly estimated by using the measured XPS peak intensities of Ni and Al with a calibration of the attenuation of photoelectrons in their travels in silica. The detailed estimation is described in the Supporting Information. For the catalysts of 2 wt % Ni-ZSM5 with filtration, 5 wt % Ni-ZSM5 with filtration, and 10 wt % Ni-ZSM5 with filtration, the Ni/Al ratio on the internal surface of micropores of ZSM5 was estimated to be 0.13, 0.32, and 0.48, respectively (Table 1). It is noted that the atomic ratio of all Ni atoms on the internal surface to that of all Al atoms on the internal surface (data of the third row in Table 1) is larger than the atomic ratio of all Ni atoms in the catalyst to all Al atoms in the catalyst (data of the first and second rows in Table 1) by about 2-fold. This suggests that Ni atoms are mainly anchored on the surface of the internal wall of micropores (Figure S1) and there is no significant thermal diffusion of Ni atoms to the wall between micropores, although the calcination was performed at a very high temperature at 550 °C.

3.2. Dispersion and Binding Environment of Ni Atoms in the Ni-Based Oxide Species on the Internal Surface of ZSM5. To identify the active sites in Ni-ZSM5, XPS spectra of Ni $2p_{3/2}$ for 10 wt % Ni-ZSM5 with filtration, in which the Ni/Al ratio on the internal surface of micropores is 0.48, were collected under various treatment conditions as noted in Figure 5. As expected, there are no NiO nanoparticles formed on the external surface of 10 wt % Ni-ZSM5 with filtration before Ar^+ sputtering (Figure 5a). The spectra before O_2 activation indicate that the Ni $2p_{3/2}$ peak is at 853.8 eV, which matches the position of the main peak of Ni^{2+} very well. It is distinctly different from the peak positions of Ni $2p_{3/2}$ of Ni^0 at 852.6 eV and Ni^{3+} at 856.1 eV as reported in the literature.[50−52] On the basis of the position of the main peaks of Ni $2p_{3/2}$ of 10 wt % Ni-ZSM5 with filtration under different conditions (Figure 5b−d), the valence state of Ni atoms in the micropores remains 2+ after activation in O_2 at 600 °C (Figure 5c) or for the catalysis of methane partial oxidation at 350 °C (Figure 5d).

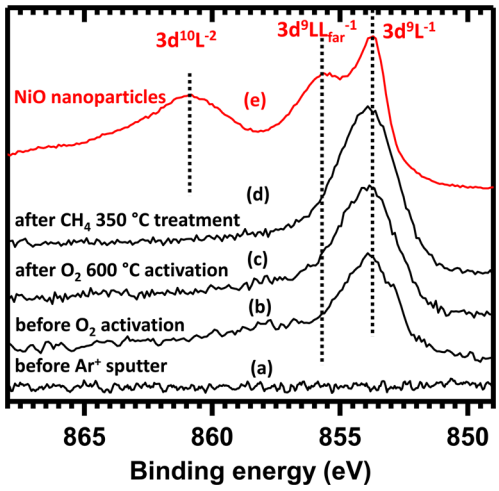

Figure 5. XPS spectra of 10 wt % Ni-ZSM5 with filtration after various treatments. For comparison, the XPS spectrum of NiO nanoparticles was also included in plot e.

The photoemission feature of Ni $2p_{3/2}$ of pure NiO nanoparticles was also included in Figure 5e. The satellite peaks at 861.0 and 856.0 eV of Ni $2p_{3/2}$ were clearly observed in the spectrum of NiO. Compared to the photoemission feature of pure NiO nanoparticles, as mentioned in section 3.1, there are no satellite peaks at 861.0 and 856.0 eV for 10 wt % Ni-ZSM5 with filtration, although Ni atoms in 10 wt % Ni-ZSM5 exhibited only the main peak of Ni^{2+} at the same position as NiO at 853.8 eV. Furthermore, even after pretreatment with 10 wt % Ni-ZSM5 with filtration at 600 °C in 1 bar of O_2 for 3 h, the photoemission feature (position and shape) of Ni $2p_{3/2}$ did not change (Figure 5c).

The absence of satellite peaks must be related to an unusual bonding environment of the Ni atom anchored to ZSM5 (Figure 6b). It is widely acknowledged that the satellite peaks of Ni $2p_{3/2}$ of Ni^{2+} of NiO result from a charge-transfer effect in photoionization.[52] Figure 6a is the crystal structure of a pure NiO nanoparticle. Before photoionization, the ground state of Ni^{2+} of NiO can be written as $3d^8L$,[52] in which L denotes the nearest ligand. After photoionization of the electrons of Ni 2p, the lowest final state is $3d^9L^{-1}$, which is formed through the electron transfer from ligand L to the Ni 3d orbital.[52] Here, L^{-1} in $3d^9L^{-1}$ denotes a hole generated on the nearest ligand due to the transfer of one electron from the ligand to the 3d orbital of Ni atom. In other words, the charging produced on Ni 2p on the photoionized Ni atom is neutralized by transferring an electron from the nearest ligand atoms to the photoionized Ni atom (d^9L^{-1}). This electronic state gives the main photoemission peak at 853.8 eV (Figure 5). In addition, two electrons of the nearest oxygen atoms could be transferred to the photoionized Ni atom. This creates another electronic state ($d^{10}L^{-2}$), which gives a satellite peak at 861.0 eV. Alternatively, the photoionized Ni atom can be neutralized by transferring an electron from one of the oxygen atoms of the second-nearest Ni atoms, Ni*-O(L_1)-Ni(L_2)-*O*(L_{far})-Ni(L_4)-O(L_5). The photoionized Ni atom is Ni*; the ligand providing an electron is *O*(L_{far});[52] this charge transfer results in a different final state labeled as $3d^9LL_{far}^{-1}$, which corresponds to the strong satellite peak at 856.0 eV (Figure 5e). In the photoemission process, the two neutralizations occur simultaneously in NiO particles. As marked in Figure 5, the main peak at 853.8 eV of Ni 2p of NiO is attributed to the final state of $3d^9L^{-1}$, while the satellite peaks

dx.doi.org/10.1021/la501184b | Langmuir 2014, 30, 8558−8569

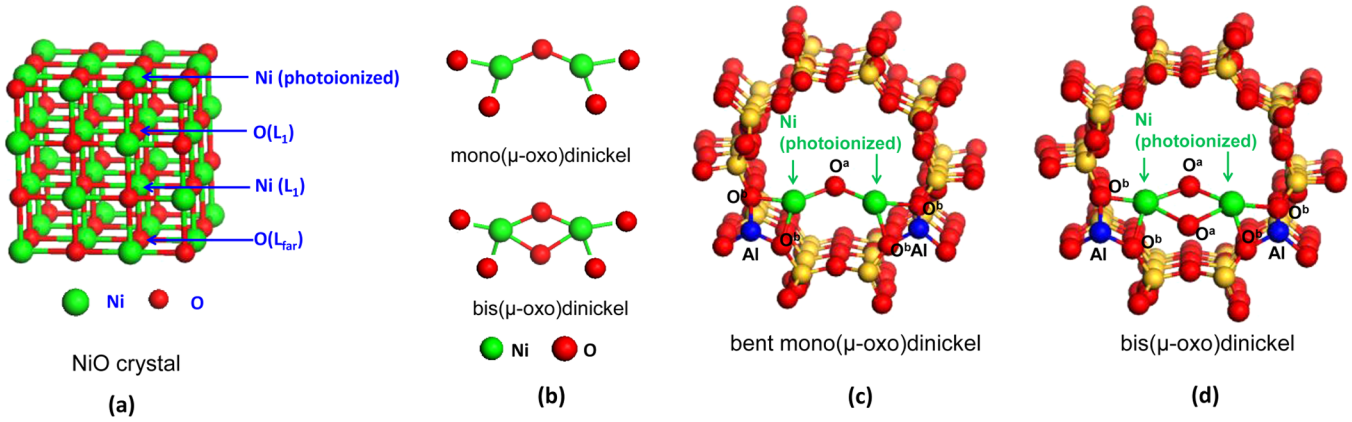

Figure 6. (a) Crystal structure of NiO. (b) Structures of mono(μ-oxo)dinickel and bis(μ-oxo)dinickel. (c) Structural model of bent mono(μ-oxo)dinickel in micropores of ZSM5. (d) Structural model of bis(μ-oxo)dinickel in micropores of ZSM5.

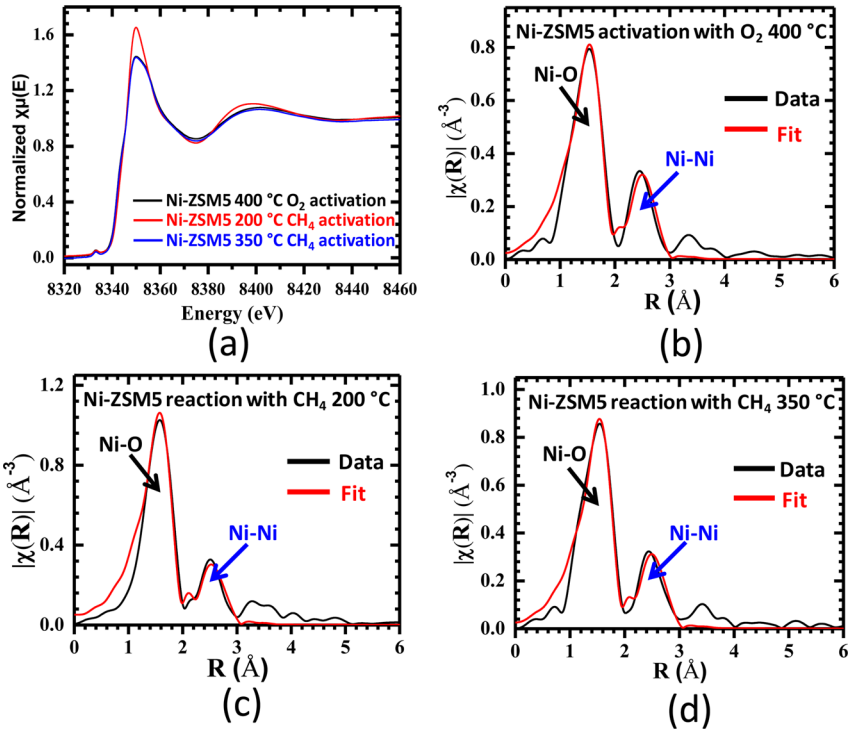

Figure 7. (a) Ni K-edge XANES spectra of 5 wt % Ni-ZSM5 with filtration during activation or catalysis. The Ni K-edge EXAFS spectra of 5 wt % Ni-ZSM5 with filtration (b) during activation with O_2 at 400 °C, (c) during catalysis with CH_4 at 200 °C, and (d) during catalysis with CH_4 at 350 °C.

at 856.0 and 861.0 eV are attributed to the final states of $3d^9LL_{far}{}^{-1}$ and $3d^{10}L^{-2}$, respectively. In the case of 10 wt % Ni-ZSM5 with filtration (Figure 5b–d), XPS spectra indicate that both the $3d^9LL_{far}{}^{-1}$ at 856.0 eV and $3d^{10}L^{-2}$ final states at 861.0 eV were missing, although the main peak of Ni 2p of Ni^{2+} at 853.8 eV attributed to $3d^9L^{-1}$ was clearly observed. As was reported in the literature, $O(L_{far})$ must be an oxygen atom in the lattice of a pure NiO particle; for example, oxygen atom $O(L_{far})$ in the La_2NiO_4 lattice cannot transfer its electron to a photoionized Ni atom to have a final state of $3d^9LL_{far}{}^{-1}$.[53] In other words, the long-range crystal structure of NiO is needed for the observation of the satellite peak at 856.0 eV.[53] The lack of final state $3d^9LL_{far}{}^{-1}$ at 856.0 eV clearly shows that there is no NiO lattice. The unusual lack of the $3d^9LL_{far}{}^{-1}$ peak at 856.0 eV in Ni $2p_{3/2}$ spectra is consistent with the coordination number of Ni atoms in the second shell to the Ni atom (Ni–O–Ni).

In-situ studies of Ni-ZSM5 during activation and catalysis using X-absorption spectroscopy were performed. Figure 7(a) presents the Ni K-edge XANES spectra of 5 wt % Ni-ZSM5 with filtration under different reaction conditions. Obviously, nickel atoms during activation in 5% O_2 and catalysis in CH_4 are in an oxidizing state. The preservation of the oxidizing state of Ni atoms is consistent with the XPS studies of 5 wt % Ni-ZSM5 after activation in O_2 (Figure 5c).

EXAFS studies of this catalyst were performed during activation of the catalysts in O_2 and the following catalysis in CH_4. Figure 7b–d are the Ni K-edge of 5 wt % Ni-ZSM5 with filtration collected during activation in O_2 and reaction with CH_4. r-space data of EXAFS of the Ni K edge (black curve) and the fitted data (red curve) are present. Table 2 lists the

dx.doi.org/10.1021/la501184b | Langmuir 2014, 30, 8558–8569

Table 2. Quantitative Analyses for Ni−O and Ni−O−Ni Contributions to the EXAFS Data Obtained Under Conditions of Activation (in O_2) and Catalysis (in CH_4)

sample	binding environment	$CN_{(O-Ni)}$	$N_{(Ni-O-Ni)}$	R(Å)	σ^2(Å^2)	ΔE_0 (eV)
O_2/400 °C	Ni−Ni′	0				
	O−Ni′	2.5 ± 0.5		2.00 ± 0.01	0.007 ± 0.002	−3.2 ± 0.8
	Ni−O−Ni′		2.0 ± 1.3	2.95 ± 0.02	0.015 ± 0.007	−3.2 ± 0.8
$CH_4$200 °C	Ni−Ni′	0				
	O−Ni′	3.0 ± 0.3		2.04 ± 0.01	0.006 ± 0.001	−3.2 ± 0.8
	Ni−O−Ni′		2.0 ± 1.1	2.99 ± 0.02	0.016 ± 0.006	−3.2 ± 0.8
CH_4 350 °C	Ni−Ni′	0				
	O−Ni′	2.5 ± 0.3		2.00 ± 0.01	0.006 ± 0.001	−3.2 ± 0.8
	Ni−O−Ni′		2.2 ± 1.1	2.95 ± 0.02	0.016 ± 0.005	−3.2 ± 0.8

coordination numbers and Ni−O bond lengths and Ni···Ni distances (the two Ni atoms are not directly bonded to each other). Clearly, there is no distinct binding between Ni and Ni atoms. The low coordination number CN_{O-Ni} is in the range of 2.5 ± 0.5 and 3.0 ± 0.3. It suggests that no NiO nanoparticles were formed on the micropores since that coordination number is equal to 6 in NiO nanoparticles (Figure 6a). In addition, the coordination of Ni atoms to the Ni atoms in the second shell (Table 2), 2.0 ± 1.1, suggests the formation of a Ni−O−Ni structure. It also excludes the possibility that −Ni−O−O−Ni− is the main oxide species since the Ni atom is found in the second-closest shell.

Both XPS and EXAFS suggest the formation of a segment structure similar to that shown in Figure 6b. Bent mono(μ-oxo)dimetal or bis(μ-oxo)dimetal (metal: Cu or Fe) (Figure 6c,d) in MMO were reported as active species for the partial oxidation of methane to methanol on a particular metalloenzymes called methane monooxygenases (MMOs).[6,54,55] Inspired by the similarity of the Ni-based oxide species revealed with XPS and EXAFS to bent mono(μ-oxo)dimetal or bis(μ-oxo)dimetal (Scheme 1), the active species in Ni-ZSM5 for the partial oxidization of CH_4 could be the anchored bent mono(μ-oxo)dinickel or bis(μ-oxo)dinickel (Figure 6c,d). The low coordination number of the Ni atom to the second shell (Ni−O−Ni) measured with EXAFS is consistent with two potential structures. The coordination number of the O to Ni atom is between 3.0 ± 0.3 and 2.5 ± 0.5 (Table 2). As the coordination number of oxygen atoms to Ni in bis(μ-oxo)dinickel is 4 (Figure 6d) instead of 3 in bent mono(μ-oxo)dinickel (Figure 6c), the bent mono(μ-oxo)dinickel (Figure 6c) is the preferred structure.

The observation of the main peak at 853.8 eV ($3d^9L^{-1}$) and the lack of the $3d^{10}L^{-2}$ satellite peak at 861.0 eV show that the oxygen atom (O^a or O^b) bonded to the Ni atom can transfer only an electron to the Ni atom. Among the two possible structures of oxide species (Figure 6c,d), the two nearest bridging oxygen atoms (O^a) in bis(μ-oxo)dinickel (Figure 6d) could transfer two electrons to the Ni atom and then give the satellite peaks at 861.0 eV for $3d^{10}L^{-2}$. Thus, the lack of a satellite peak at 861.0 makes us exclude the bis(μ-oxo)dinickel (Figure 6d). Furthermore, for the bis(μ-oxo)dinickel structure, the oxidation state of Ni was considered to be the Ni^{3+} state in the literature.[56,57] The main peak of Ni $2p_{3/2}$ at Ni^{3+} is 856.1 eV instead of 853.8 eV.[51,52] The observed peak at 853.8 eV in Figure 5b−d shows that the valence state of the Ni atom in the Ni-based oxide structure formed in ZSM5 is not 3+. Thus, the observation of the main peak at 853.8 eV and the lack of any satellite peaks of Ni $2p_{3/2}$ in Ni-ZSM5 suggest that the Ni-based oxide structure formed on the internal surface of the micropores is very likely the bent mono(μ-oxo)dinickel structure instead of the bis(μ-oxo)dinickel and a NiO nanoparticle.

It is noteworthy that the photoemission feature of Ni 2p for the samples of 10 wt % Ni-ZSM5 with filtration is very similar to that of samples of 2.5 wt % Ni-ZSM5 with filtration, 2.5 wt % Ni-ZSM5 without filtration after sputtering, 5 wt % Ni-ZSM5 with filtration (not shown here), and 5 wt % Ni-ZSM5 without filtration after sputtering (not shown here). This indicates that likely identical bent mono(μ-oxo)dinickel structures were formed in the samples with different Ni concentrations in micropores of ZSM5. Therefore, the samples characterized with various techniques are representative of active structure of Ni-ZSM5, although the Ni concentrations in micropores of ZSM5 are different in some cases.

The formation of this specific Ni-based oxide structure was further confirmed by UV−vis studies. As shown in Figure 8aa, the absorption band centered at 22 800 cm^{-1} appeared for 5 wt % Ni-ZSM5 with filtration activated in O_2 at 600 °C. However, this band was lacking in Ni-ZSM5 without activation at 600 °C (Figures 8ab and 4a−c). Obviously, the activation at 600 °C in O_2 gave rise to the absorption band at 22 800 cm^{-1}. UV−vis of a pure H-ZSM5 upon activation at 600 °C in O_2 was collected in Figure 8ac. As shown in Figure 8ac, in fact there is no absorption band in the region close to 22 800 cm^{-1}. It is noted that an absorption band of the bis(μ-oxo)dinickel structure at ∼25 000 cm^{-1} was reported in the literature.[56] The lack of a band at ∼25 000 cm^{-1} excluded the bis(μ-oxo)dinickel structure in the Ni-ZSM5 catalyst. Therefore, absorption at 22 800 cm^{-1} for Ni-ZSM5 was assigned to the feature of bent mono(μ-oxo)dinickel formed in the process of activation in O_2. Figure 8b presents a time-dependent decrease in the intensity of this absorption band at 22 800 cm^{-1} along with the consumption of the oxygen atoms of the bent mono(μ-oxo)dinickel and the formation of products, to be discussed in the following paragraphs. This suggests that the bent mono(μ-oxo)dinickel is the active site for methane partial oxidation to methanol.

It is noted that XRD, TEM, XPS, and UV−vis characterizations indicate that NiO nanoclusters can form on the external surface of ZSM5, while the bent mono(μ-oxo)dinickel structure is formed on the internal surface of ZSM5. The precursor of NiO nanoclusters on the external surface of ZSM5 is introduced in the incipient wetness impregnation process, while the precursor of the bent mono(μ-oxo)dinickel structure is introduced through the ion-exchange process of H ions in H-ZSM5 with Ni ions in solution. After calcination, the precursor on the external surface of ZSM forms NiO nanoclusters. The precursor in ZSM5 formed a bent mono(μ-oxo)dinickel

dx.doi.org/10.1021/la501184b | Langmuir 2014, 30, 8558−8569

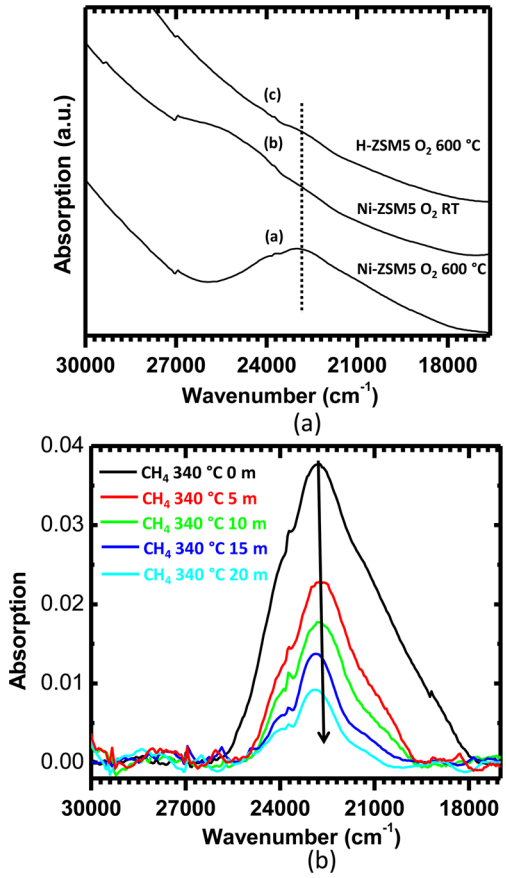

Figure 8. (a) In-situ UV−vis spectra of 5 wt % Ni-ZSM5 with filtration after O_2 treatment at RT and 600 °C. For comparison, the spectrum of H-ZSM5 after O_2 treatment at 600 °C was included as well. (b) Time-dependent decrease in the intensity of the absorption band at 22 800 cm^{-1} along the interaction with CH_4 at 340 °C after various amounts of time.

structure upon calcination. For a ZSM5 with both external NiO nanoclusters and internal bent mono(μ-oxo)dinickel structure, a sputtering will remove the external NiO nanoclusters. A single peak of Ni $2p_{3/2}$ without a satellite appears after sputtering since only Ni $2p_{3/2}$ of NiO nanoclusters exhibits a satellite peak.

3.3. Catalytic Performance. Methane conversion on activated Ni-ZSM5 produces CH_3OH (main product) and HCOOH and $HOCH_2CH_2OH$. The amounts of products including CH_3OH, HCOOH, and $HOCH_2CH_2OH$ were determined by quantitative analysis using NMR. The quantitative analyses of the concentrations of these potential products by using NMR are described in the Experimental Section and Supporting Information. As clearly shown in Tables S1 and S4, blank experiments using pure ZSM5 show that pure ZSM5 is not active in the conversion of CH_4 to CH_3OH or other oxygenates at all. Because extraction and centrifugation steps were also applied to the blank experiments on pure ZSM5 (Tables S1 and S4) and there was no methanol or formic acid formed, clearly the extraction and centrifugation steps did not introduce any CH_3OH or formic acid into the system during separation and measurements.

The yield of CH_3OH on 5 wt % Ni-ZSM5 with filtration at 175 °C upon activation at 650 °C with pure O_2 is 2.0 μmol per gram of the catalyst. Here the weight of the catalyst is defined with respect to the total nickel and ZSM5. To understand the formation mechanism of the specific oxide with the purpose of maximizing the available sites in terms of the number of bent mono(μ-oxo)dinickel species, parallel studies of six catalysts (2 wt % Ni-ZSM5 without filtration, 5 wt % Ni-ZSM5 without filtration, 10 wt % Ni-ZSM5 without filtration, 2 wt % Ni-ZSM5 with filtration, 5 wt % Ni-ZSM5 with filtration, and 10 wt % Ni-ZSM5 with filtration) were performed. For 2 wt % Ni-ZSM5 without filtration, 5 wt % Ni-ZSM5 without filtration, and 10 wt % Ni-ZSM5 without filtration, the surfaces of these catalysts after activation in O_2 were sputtered until all NiO nanoparticles were removed. Then, XPS was performed on the six catalysts to measure their Ni/Al atomic ratios. Figure 9 presents the yields

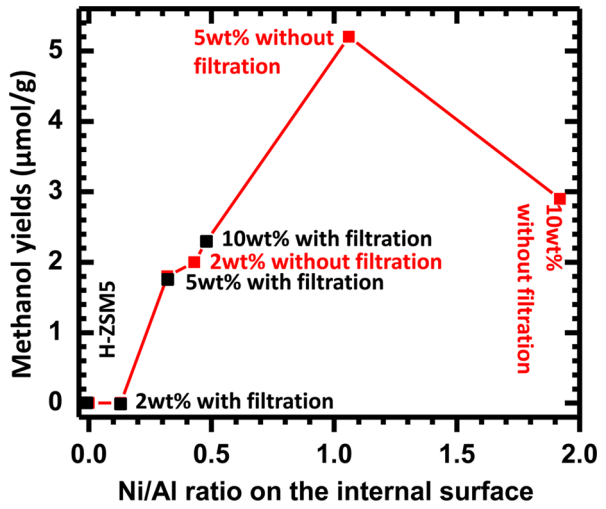

Figure 9. Methanol yields as a function of the atomic ratio of Ni/Al on the internal surfaces of micropores for different Ni-ZSM5 catalysts. The catalysts were first activated with pure O_2 at 650 °C for 3 h and then catalyzed with CH_4 at 175 °C for 45 min.

of CH_3OH on these catalysts as a function of their calculated Ni/Al atomic ratio on the internal surfaces of micropores of catalysts. For Ni-ZSM5 without filtration, 5 wt % Ni-ZSM5 without filtration exhibited a higher yield than 2 wt % Ni-ZSM5 without filtration and 10 wt % Ni-ZSM5 without filtration. The yield of CH_3OH on 5 wt % Ni-ZSM5 without filtration is 5.1 μmol per gram of this catalyst (Figure 9). Interestingly, for 5 wt % Ni-ZSM5 without filtration, the overall Ni/Al ratio on the internal surfaces of micropores is approximately 1, suggesting that Ni oxide species are formed at the sites of Al atoms. The Ni/Al atomic ratio of 10 wt % Ni-ZSM5 is about 2.0. However, the yield of CH_3OH on 10 wt % Ni-ZSM5 decreases. It suggests that some Ni atoms could form a different type of oxide species or even small NiO nanoparticles in the pores. Thus, a compromise concentration of 5 wt % gave the highest yield of CH_3OH for Ni-ZSM5 without filtration (Figure 9).

Figure 9 presents the yields in terms of the activity of two series of Ni-ZSM5 catalysts: Ni-ZSM5 without filtration (red squares) and Ni-ZSM5 with filtration (black square). Compared to the series of Ni-ZSM5 without filtration (2 wt % Ni-ZSM5 without filtration, 5 wt % Ni-ZSM5 without filtration, and 10 wt % Ni-ZSM5 without filtration), the series of Ni-ZSM5 with filtration (2 wt % Ni-ZSM5 with filtration, 5 wt % Ni-ZSM5 with filtration, and 10 wt % Ni-ZSM5 with filtration) exhibited a relatively low yields compared to those without filtration (2 wt % Ni-ZSM5 without filtration, 5 wt % Ni-ZSM5 without filtration, and 10 wt % Ni-ZSM5 without filtration). These lower yields of Ni-ZSM5 with filtration

dx.doi.org/10.1021/la501184b | Langmuir 2014, 30, 8558−8569

suggest that the filtration step removed not only the extra Ni^{2+} species left on the external surface of ZSM5 particles but also some Ni^{2+} ions on the internal surface of those micropores. As the series of Ni-ZSM5 without filtration (red squares in Figure 9) exhibited a larger yield of CH_3OH than the corresponding ones with filtration (black squares in Figure 9), all of the following catalysis studies were performed on catalysts of Ni-ZSM5 without filtration.

In optimizing the activation temperature, oxidizing gas, and reaction temperature of catalysis, a reaction was performed (1) at different reaction temperatures after activation at a specific temperature or (2) at a specific catalysis temperature after activation at different temperatures. Efforts were made to find the best activation temperature and catalysis temperature which give the highest activity. As shown in entry 2-5 of Table S1, catalysis was performed on three catalysts: 2 wt % Ni-ZSM5 without filtration, 5 wt % Ni-ZSM5 without filtration, and 10 wt % Ni-ZSM5 without filtration under the same activation condition (5% O_2 at 550 °C) and temperature (175 °C). These parallel studies showed that 5 wt % Ni-ZSM5 without filtration gave the highest yield. For these three catalysts, their catalysis was performed at a higher catalysis temperature, 200 °C (entry 5-7 in Table S1). Similar to the catalysis at 175 °C, catalysis at 200 °C on 5 wt % Ni-ZSM5 without filtration exhibited the highest yield among 2 wt % Ni-ZSM5 without filtration, 5 wt % Ni-ZSM5 without filtration, and 10 wt % Ni-ZSM5 without filtration. This is consistent with the higher Ni/Al atomic ratio in 5 wt % Ni-ZSM5 compared to that in 2 wt % Ni-ZSM5, while for 10 wt % Ni-ZSM5 the formed NiO may significantly block the opening of pores of ZSM5 for CH_4. Further optimization of the activation temperature in 5% O_2 was done by measuring the yields of CH_3OH produced from 5% Ni-ZSM5 without filtration activated at different temperatures in 5% O_2. The yields in these experiments are listed in the Supporting Information (Table S2). These parallel studies in Table S2 showed that the best activation temperature is 650 °C (entry 5 in Table S2). The best catalysis temperature was found by performing catalysis at different temperatures on 5 wt % Ni-ZSM5 activated at 650 °C in 5% O_2 (Table S3). In fact, the highest yield and best selectivity for the production of CH_3OH were achieved at a catalysis temperature of 175 °C.

Further investigations of catalysts activated in pure O_2 at 650 °C (the optimized activation temperature found above) followed by catalysis at 175 °C (the best reaction temperature found above) were performed (Table S4). It is interesting that the total yield for a catalyst activated in pure O_2 at 650 °C is double in contrast to that for activation in 5% O_2. The main increase in the products was the yield of HCOOH whereas the yield of CH_3OH was nearly unchanged. In addition, a new product, $HOCH_2CH_2OH$, was identified for catalysis on the catalyst activated in pure O_2 at 650 °C. Ethylene glycol, $HOCH_2CH_2OH$, could be produced from ethylene oxide since it reacts with water to produce ethylene glycol.[58] Ethylene oxide can be formed from the oxidation of ethylene.[58] Ethylene might be produced from the oxidative coupling of methane.[59,60] In this reaction process, methane can be activated on the catalyst surface, forming methyl free radicals which have the possibility to couple with each other to form ethane (C_2H_6). Then the ethane can subsequently undergo dehydrogenation to form ethylene (C_2H_4). The ethylene can be oxidized to form ethylene oxide. Therefore, ethylene glycol can be formed after the hydrolysis of ethylene oxide with water.

Note that during catalysis at 175 °C or 200 °C, the online GC measurements show that there are no oxygenates in the gas phase. In fact, the formed methanol and the other oxygenate are adsorbed on the internal wall of ZSM5. As mentioned in the Experimental Section, hydrolysis is included to extract products formed inside the micropores of zeolites. Furthermore, no formations of CO or CO_2 were detected in the gaseous phase based on the online GC measurements during catalysis.

For 5 wt % Ni-ZSM5 without filtration activated in pure O_2 at 650 °C followed by catalysis at 175 °C, the total yield of oxygenates is ~15.0 μmol per gram of catalyst. On the basis of the XPS measurement of the Ni/Al ratio (Table 1 and Figure 9), the amount of Ni on the internal surface of ZSM5 can be estimated to be 250 μmol per gram of catalyst for 5 wt % Ni-ZSM5 (without filtration). Assuming that the stoichiometric ratio of consumed bridged oxygen atoms in bent mono(μ-oxo)dinickel in ZSM5 to the total formed methanol and formic acid is 2:1, one could calculate that 12% of the bridging oxygen atoms of bent mono(μ-oxo)dinickel (Figure 6c) participate in the partial oxidation of methane to methanol or formic acid.

The total yield of oxygenates at ~15.0 μmol per gram of catalyst for Ni-ZSM5 is higher than that reported for Cu-ZSM5, in which ~9 μmol of methanol per gram of catalyst was reported.[21] Ni-ZSM5 and Cu-ZSM5 were activated through annealing in O_2. In the case of Fe-ZSM5, a total yield of oxygenates of ~60 μmol per gram of catalyst was reported[20] upon Fe-ZSM5 activation through N_2O. Activation in O_2 is a convenient and economical process for generating the catalyst for this conversion.

3.4. Kinetics Studies of the Direct Oxidation of Methane. The formation of the bent mono(μ-oxo)dinickel species during activation in O_2 at high temperatures was further confirmed by the observation of an absorption band at 22 800 cm^{-1}. As clearly shown in Figure 8b, the peak intensity of the absorption band of the bent mono(μ-oxo)dinickel decreases along the increase in reaction time. Quantification of the formed products after different extents of reaction suggests that more methanol was produced after the reaction for a longer time. These studies confirm that bent mono(μ-oxo)dinickel is the active site for the CH_4 conversion to CH_3OH.

Kinetic studies of the direct conversion of CH_4 to CH_3OH were performed by measuring the amount of the left bent mono(μ-oxo)dinickel at different temperature using UV−vis. The kinetic studies were performed in the temperature range of 280−330 °C to evaluate the activation barrier (E_a) for the reaction of oxygen-activated Ni-ZSM5 with CH_4. Upon activation in O_2 at 600 °C, the catalyst was a fresh catalyst. The absorption band at 22 800 cm^{-1} was measured in O_2 at 280 °C; the intensity of this absorption band is termed $A_{T(O_2)}$, where T refers to a reaction temperature. Then CH_4 was introduced to the catalyst at this temperature, and the absorption spectrum was collected 5 minutes after the introduction of CH_4 at this temperature. The intensity of the band at 22 800 cm^{-1} 5 minutes after CH_4 was introduced is termed $A_{T(\text{after 5 min in } CH_4)}$. The difference between the intensity of the band of bent mono(μ-oxo)dinickel (22 800 cm^{-1}) before the introduction of CH_4 and that after 5 minutes of reaction is proportional to the reacted species of bent mono(μ-oxo)-dinickel, $\Delta A_{T(\text{reacted})} = A_{T(O_2)} - A_{T(\text{after 5 min in } CH_4)}$. Then, the conversion at this temperature can be calculated with the following equation:

dx.doi.org/10.1021/la501184b | Langmuir 2014, 30, 8558−8569

$$X = \frac{\Delta A_T(\text{reacted})}{A_T(O_2)} = \frac{A_T(O_2) - A_T(\text{after 5 min in } CH_4)}{A_T(O_2)} \quad (1)$$

The conversion (X) at a temperature between 280 and 330 °C was controlled in the kinetic control regime (lower than 15%). After this UV−vis measurement at 280 °C, the catalyst was heated to 600 °C in pure O_2 to desorb or/and combust the products, followed by activation in O_2 for a half hour for the regeneration of this catalyst. The regenerated catalyst was cooled to 290 °C in O_2, and the absorption band at 22 800 cm^{-1} was collected at this temperature. This absorption band gives A_{290,O_2}. Then, CH_4 was introduced, and the absorption band was taken after 5 minutes at 290 °C to get $A_{290(\text{after 5 min in } CH_4)}$. The conversion of CH_4 at 290 °C was calculated with eq 1, as used for 280 °C described above. Parallel studies were performed at 300, 310, 320, and 330 °C. The conversion in this temperature range (280−330 °C) allowed us to plotting the $\ln(X)$ as a function of $1/T$. Figure S4 is the Arrhenius plot of the conversion versus the reciprocal temperature in Kelvin. The activation energy calculated from the slope is 83.2 kJ/mol.

SUMMARY

A bent mono(μ-oxo)dinickel structure anchored on the internal surface of micropores of ZSM5 was synthesized by incipient wetness impregnation following activation in O_2. This catalyst is active for the direct oxidation of methane to methanol at a reaction temperature as low as 150 °C at ambient pressure for CH_4. The total yield of CH_3OH, HCOOH, and $HOCH_2CH_2OH$ on a gram of ZSM5 catalyst anchored with bent mono(μ-oxo)dinickel structure under mild conditions (175 °C in 1 bar CH_4) is 14.9 μmol. In-situ studies using UV−vis, EXAFS, and XPS revealed that the bent mono(μ-oxo)dinickel structure is the active site. It is a new structure active for the direct partial oxidation of methane to methanol. The bent mono(μ-oxo)dinickel catalyzes the direct oxidation of methane to methanol through an activation barrier of 83.2 kJ/mol.

ASSOCIATED CONTENT

Supporting Information

Estimation of the atomic ratio of Ni and Al atoms on the internal surface of micropores of ZSM5. This material is available free of charge via the Internet at http://pubs.acs.org.

AUTHOR INFORMATION

Corresponding Author

*E-mail: ftao@nd.edu.

Author Contributions

J.S., W.H., and L.N. made equal contributions to this work.

Notes

The authors declare no competing financial interest.

ACKNOWLEDGMENTS

This work is partially supported by the Chemical Sciences, Geosciences, and Biosciences Division, Office of Basic Energy Sciences, Office of Science, U.S. Department of Energy under grant no. DE-FG02-12ER16353. A.I.F. acknowledges support from U.S. Department of Energy grant no. DE-FG02-03ER15476. Beamlines X19A and X18B at the NSLS are supported in part by the Synchrotron Catalysis Consortium, U.S. Department of Energy grant no. DE-FG02-05ER15688.

REFERENCES

(1) Behrens, M.; Studt, F.; Kasatkin, I.; Kuhl, S.; Havecker, M.; Abild-Pedersen, F.; Zander, S.; Girgsdies, F.; Kurr, P.; Kniep, B. L.; Tovar, M.; Fischer, R. W.; Norskov, J. K.; Schlogl, R. The Active Site of Methanol Synthesis over $Cu/ZnO/Al_2O_3$ Industrial Catalysts. *Science* **2012**, *336*, 893−897.

(2) Hueso, J. L.; Martinez-Martinez, D.; Caballero, A.; Gonzalez-Elipe, A. R.; Mun, B. S.; Salmeron, M. Near-ambient X-ray photoemission spectroscopy and kinetic approach to the mechanism of carbon monoxide oxidation over lanthanum substituted cobaltites. *Catal. Commun.* **2009**, *10*, 1898−1902.

(3) Vandentop, G. J.; Kawasaki, M.; Nix, R. M.; Brown, I. G.; Salmeron, M.; Somorjai, G. A. Formation of Hydrogenated Amorphous-Carbon Films of Controlled Hardness from a Methane Plasma. *Phys. Rev. B* **1990**, *41*, 3200−3210.

(4) Coperet, C. C-H Bond Activation and Organometallic Intermediates on Isolated Metal Centers on Oxide Surfaces. *Chem. Rev.* **2010**, *110*, 656−680.

(5) Ding, X. L.; Wu, X. N.; Zhao, Y. X.; He, S. G. C-H Bond Activation by Oxygen-Centered Radicals over Atomic Clusters. *Acc. Chem. Res.* **2012**, *45*, 382−390.

(6) Elliott, S. J.; Zhu, M.; Tso, L.; Nguyen, H. H. T.; Yip, J. H. K.; Chan, S. I. Regio- and stereoselectivity of particulate methane monooxygenase from Methylococcus capsulatus (Bath). *J. Am. Chem. Soc.* **1997**, *119*, 9949−9955.

(7) Culpepper, M. A.; Rosenzweig, A. C. Architecture and active site of particulate methane monooxygenase. *Crit. Rev. Biochem. Mol. Biol.* **2012**, *47*, 483−492.

(8) Shiota, Y.; Juhasz, G.; Yoshizawa, K. Role of Tyrosine Residue in Methane Activation at the Dicopper Site of Particulate Methane Monooxygenase: A Density Functional Theory Study. *Inorg. Chem.* **2013**, *52*, 7907−7917.

(9) Turitsyna, E. A.; Trukhan, V. M.; Shteinman, A. A. Synthesis and structure of binuclear iron(II) complex with the cage-like ligand as a model of methane monooxygenase. *Russ. Chem. Bull.* **2012**, *60*, 2088−2093.

(10) Basch, H.; Musaev, D. G.; Morokuma, K. A density functional study of the completion of the methane monooxygenase catalytic cycle. Methanol complex to MMOH resting state. *J. Phys. Chem. B* **2001**, *105*, 8452−8460.

(11) Brantner, C. A.; Remsen, C. C.; Owen, H. A.; Buchholz, L. A.; Collins, M. L. P. Intracellular localization of the particulate methane monooxygenase and methanol dehydrogenase in Methylomicrobium album BGS. *Arch. Microbiol.* **2002**, *178*, 59−64.

(12) Henckel, T.; Friedrich, M.; Conrad, R. Molecular analyses of the methane-oxidizing microbial community in rice field soil by targeting the genes of the 16S rRNA, particulate methane monooxygenase, and methanol dehydrogenase. *Appl. Environ. Microbiol.* **1999**, *65*, 1980−1990.

(13) Yoshizawa, K.; Suzuki, A.; Shiota, Y.; Yamabe, T. Conversion of methane to methanol on diiron and dicopper enzyme models of methane monooxygenase: A theoretical study on a concerted reaction pathway. *Bull. Chem. Soc. Jpn.* **2000**, *73*, 815−827.

(14) Hammond, C.; Conrad, S.; Hermans, I. Oxidative Methane Upgrading. *ChemSusChem* **2012**, *5*, 1668−1686.

(15) Schwarz, H. Chemistry with Methane: Concepts Rather than Recipes. *Angew. Chem., Int. Ed.* **2011**, *50*, 10096−10115.

(16) Beznis, N. V.; Weckhuysen, B. M.; Bitter, J. H. Partial Oxidation of Methane Over Co-ZSM-5: Tuning the Oxygenate Selectivity by Altering the Preparation Route. *Catal. Lett.* **2010**, *136*, 52−56.

(17) Beznis, N. V.; van Laak, A. N. C.; Weckhuysen, B. M.; Bitter, J. H. Oxidation of methane to methanol and formaldehyde over Co-ZSM-5 molecular sieves: Tuning the reactivity and selectivity by alkaline and acid treatments of the zeolite ZSM-5 agglomerates. *Microporous Mesoporous Mater.* **2011**, *138*, 176−183.

(18) Kung, M. C.; Lin, S. S. Y.; Kung, H. H. In situ Infrared Spectroscopic Study of CH_4 Oxidation Over Co-ZSM-5. *Top. Catal.* **2012**, *55*, 108−115.
(19) Hammond, C.; Forde, M. M.; Ab Rahim, M. H.; Thetford, A.; He, Q.; Jenkins, R. L.; Dimitratos, N.; Lopez-Sanchez, J. A.; Dummer, N. F.; Murphy, D. M.; Carley, A. F.; Taylor, S. H.; Willock, D. J.; Stangland, E. E.; Kang, J.; Hagen, H.; Kiely, C. J.; Hutchings, G. J. Direct Catalytic Conversion of Methane to Methanol in an Aqueous Medium by using Copper-Promoted Fe-ZSM-5. *Angew. Chem., Int. Ed.* **2012**, *51*, 5129−5133.
(20) Starokon, E. V.; Parfenov, M. V.; Pirutko, L. V.; Abornev, S. I.; Panov, G. I. Room-Temperature Oxidation of Methane by alpha-Oxygen and Extraction of Products from the FeZSM-5 Surface. *J. Phys. Chem. C* **2011**, *115*, 2155−2161.
(21) Groothaert, M. H.; Smeets, P. J.; Sels, B. F.; Jacobs, P. A.; Schoonheydt, R. A. Selective oxidation of methane by the bis(mu-oxo)dicopper core stabilized on ZSM-5 and mordenite zeolites. *J. Am. Chem. Soc.* **2005**, *127*, 1394−1395.
(22) Woertink, J. S.; Smeets, P. J.; Groothaert, M. H.; Vance, M. A.; Sels, B. F.; Schoonheydt, R. A.; Solomon, E. I. A $[Cu_2O]^{(2+)}$ core in Cu-ZSM-5, the active site in the oxidation of methane to methanol. *Proc. Natl. Acad. Sci. U.S.A.* **2009**, *106*, 18908−18913.
(23) Vanelderen, P.; Hadt, R. G.; Smeets, P. J.; Solomon, E. I.; Schoonheydt, R. A.; Sels, B. F. Cu-ZSM-5: A biomimetic inorganic model for methane oxidation. *J. Catal.* **2011**, *284*, 157−164.
(24) Xu, J.; Zheng, A. M.; Wang, X. M.; Qi, G. D.; Su, J. H.; Du, J. F.; Gan, Z. H.; Wu, J. F.; Wang, W.; Deng, F. Room temperature activation of methane over Zn modified H-ZSM-5 zeolites: Insight from solid-state NMR and theoretical calculations. *Chem. Sci.* **2012**, *3*, 2932−2940.
(25) Mckay, D.; Hargreaves, J. S. J.; Howe, R. F. XPS evidence for molybdenum nitride formation in ZSM-5. *Catal. Lett.* **2006**, *112*, 109−113.
(26) Wang, L.; Zhang, S. R.; Zhu, Y.; Patlolla, A.; Shan, J. J.; Yoshida, H.; Takeda, S.; Frenkel, A. I.; Tao, F. Catalysis and In Situ Studies of Rh-1/Co_3O_4 Nanorods in Reduction of NO with H-2. *ACS Catal.* **2013**, *3*, 1011−1019.
(27) Zhu, Y.; Zhang, S. R.; Shan, J. J.; Nguyen, L.; Zhan, S. H.; Gu, X. L.; Tao, F. In Situ Surface Chemistries and Catalytic Performances of Ceria Doped with Palladium, Platinum, and Rhodium in Methane Partial Oxidation for the Production of Syngas. *ACS Catal.* **2013**, *3*, 2627−2639.
(28) Shan, J. J.; Zhu, Y.; Zhang, S. R.; Zhu, T.; Rouvimov, S.; Tao, F. Catalytic Performance and in Situ Surface Chemistry of Pure alpha-MnO2 Nanorods in Selective Reduction of NO and N2O with CO. *J. Phys. Chem. C* **2013**, *117*, 8329−8335.
(29) Zhang, S. R.; Shan, J. J.; Zhu, Y.; Frenkel, A. I.; Patlolla, A.; Huang, W. X.; Yoon, S. J.; Wang, L.; Yoshida, H.; Takeda, S.; Tao, F. WGS Catalysis and In Situ Studies of CoO_{1-x}, PtCon/Co_3O_4, and PtmCom '/CoO_{1-x} Nanorod Catalysts. *J. Am. Chem. Soc.* **2013**, *135*, 8283−8293.
(30) Zhang, S. R.; Shan, J. J.; Zhu, Y.; Nguyen, L.; Huang, W. X.; Yoshida, H.; Takeda, S.; Tao, F. Restructuring Transition Metal Oxide Nanorods for 100% Selectivity in Reduction of Nitric Oxide with Carbon Monoxide. *Nano Lett.* **2013**, *13*, 3310−3314.
(31) Grzesiek, S.; Bax, A. The Importance of Not Saturating H2o in Protein Nmr - Application to Sensitivity Enhancement and Noe Measurements. *J. Am. Chem. Soc.* **1993**, *115*, 12593−12594.
(32) Nashner, M. S.; Frenkel, A. I.; Adler, D. L.; Shapley, J. R.; Nuzzo, R. G. Structural characterization of carbon-supported platinum-ruthenium nanoparticles from the molecular cluster precursor PtRu5C(CO)(16). *J. Am. Chem. Soc.* **1997**, *119*, 7760−7771.
(33) Frenkel, A. I.; Hills, C. W.; Nuzzo, R. G. A view from the inside: Complexity in the atomic scale ordering of supported metal nanoparticles. *J. Phys. Chem. B* **2001**, *105*, 12689−12703.
(34) Sanchez, S. I.; Menard, L. D.; Bram, A.; Kang, J. H.; Small, M. W.; Nuzzo, R. G.; Frenkel, A. I. The Emergence of Nonbulk Properties in Supported Metal Clusters: Negative Thermal Expansion and Atomic Disorder in Pt Nanoclusters Supported on γ-Al_2O_3. *J. Am. Chem. Soc.* **2009**, *131*, 7040−7054.
(35) Casu, M.; Lai, A.; Musinu, A.; Piccaluga, G.; Solinas, S.; Bruni, S.; Cariati, F.; Beretta, E. XRD, TEM, IR and Si-29 MAS NMR characterization of NiO-SiO2 nanocomposites. *J. Mater. Sci.* **2001**, *36*, 3731−3735.
(36) Grinys, T.; Tamulevicius, S.; Prosycevas, I.; Meskinis, S. XRD Analysis of Plasma Sprayed YSZ-NiO-Ni Ceramic Coatings. *Plasma Processes and Polymers* **2007**, *4*, S181−S184.
(37) Rao, M. V.; Sturm, S.; Phillipp, F.; Zinkevich, M. XRD and TEM study of NiO-LSGM reactivity. *International Journal of Materials Research* **2006**, *97*, 789−793.
(38) Dai, F. Y.; Suzuki, M.; Takahashi, H.; Saito, Y. XRD characteristics of NA-ZSM-5 synthesized from an organic-free system. *Bull. Chem. Soc. Jpn.* **1988**, *61*, 3403−3407.
(39) Kosslick, H.; Tuan, V. A.; Fricke, R.; Peuker, C. IR-investigations and XRD-investigations on isomorphous substituted ZSM-5 zeolites. *Ber. Bunsen-Ges. Phys. Chem. Chem. Phys.* **1992**, *96*, 1761−1765.
(40) Peck, M. A.; Langell, M. A. Comparison of Nanoscaled and Bulk NiO Structural and Environmental Characteristics by XRD, XAFS, and XPS. *Chem. Mater.* **2012**, *24*, 4483−4490.
(41) Preda, I.; Mossanek, R. J. O.; Abbate, M.; Alvarez, L.; Mendez, J.; Gutierrez, A.; Soriano, L. Surface contributions to the XPS spectra of nanostructured NiO deposited on HOPG. *Surf. Sci.* **2012**, *606*, 1426−1430.
(42) Tyuliev, G. T.; Kostov, K. L. XPS/HREELS study of NiO films grown on Ni(111). *Phys. Rev. B* **1999**, *60*, 2900−2907.
(43) Bagus, P. S.; Pacchioni, G.; Parmigiani, F. Final-state effects for the core-level XPS spectra of NiO. *Chem. Phys. Lett.* **1993**, *207*, 569−574.
(44) Hegde, M. S.; Kumar, T. S. S.; Mallya, R. M. XPS, UPS and AES study of surface segregation and oxidation of Ni-Ru alloy - evidence for decrease in dissociation temperature of NiO in the presence of Ru. *Surf. Sci.* **1987**, *188*, 255−266.
(45) Sanz, J. M.; Tyuliev, G. T. An XPS study of thin NiO films deposited on MgO(100). *Surf. Sci.* **1996**, *367*, 196−202.
(46) Scharfschwerdt, C.; Kutscher, J.; Schneider, F.; Neumann, M.; Tougaard, S. Quantitative XPS of NiO, CoO and MnO - the effects of elastic and inelastic electron-scattering. *J. Electron Spectrosc. Relat. Phenom.* **1992**, *60*, 321−335.
(47) Xiong, G. X.; Tan, C. Q.; Wang, H. L. Study of reduction behaviours of molybdena on MoO(3)/Al(2)O(3), MoO(3)/TiO(2) and NiO-MoO(3)/TiO(2) systems by XPS. *Acta Phys. Chim. Sinica* **1989**, *5*, 370−376.
(48) Langell, M. A.; Nassir, M. H. Stabilization of NiO(111) thin-films by surface hydroxyls. *J. Phys. Chem.* **1995**, *99*, 4162−4169.
(49) Wang, Y. P.; Zhu, J. W.; Zhang, L. L.; Yang, X. J.; Lu, L. D.; Wang, X. Study on the preparation and spectral characteristics of Nano-NiO. *Spectrosc Spect Anal* **2006**, *26*, 690−693.
(50) Salvati, L.; Makovsky, L. E.; Stencel, J. M.; Brown, F. R.; Hercules, D. M. Surface Spectroscopic Study of Tungsten-Alumina Catalysts Using X-Ray Photo-Electron, Ion-Scattering, and Raman Spectroscopies. *J. Phys. Chem.* **1981**, *85*, 3700−3707.
(51) Carley, A. F.; Jackson, S. D.; O'Shea, J. N.; Roberts, M. W. The formation and characterisation of Ni3+ - an X-ray photoelectron spectroscopic investigation of potassium-doped Ni(110)-O. *Surf. Sci.* **1999**, *440*, L868−L874.
(52) Grosvenor, A. P.; Biesinger, M. C.; Smart, R. S.; McIntyre, N. S. New interpretations of XPS spectra of nickel metal and oxides. *Surf. Sci.* **2006**, *600*, 1771−1779.
(53) Sangaletti, L.; Depero, L. E.; Parmigiani, F. On the non-local screening mechanisms in the 2p photoelectron spectra of NiO and La_2NiO_4. *Solid State Commun.* **1997**, *103*, 421−424.
(54) Vanelderen, P.; Smeets, P. J.; Hadt, R. G.; Woertink, J. S.; Schoonheydt, R. A.; Sels, B. F.; Solomon, E. I. Oxygen precursor to the reactive intermediate in methanol synthesis by Cu-ZSM-5. *Abstr. Pap. Am. Chem. Soc.* **2011**, 242.

(55) Balasubramanian, R.; Smith, S. M.; Rawat, S.; Yatsunyk, L. A.; Stemmler, T. L.; Rosenzweig, A. C. Oxidation of methane by a biological dicopper centre. *Nature* **2010**, *465*, 115−U131.
(56) Itoh, S.; Bandoh, H.; Nakagawa, M.; Nagatomo, S.; Kitagawa, T.; Karlin, K. D.; Fukuzumi, S. Formation, characterization, and reactivity of bis(mu-oxo)dinickel(III) complexes supported by a series of bis[2-(2-pyridyl)ethyl]amine ligands. *J. Am. Chem. Soc.* **2001**, *123*, 11168−11178.
(57) Honda, K.; Cho, J.; Matsumoto, T.; Roh, J.; Furutachi, H.; Tosha, T.; Kubo, M.; Fujinami, S.; Ogura, T.; Kitagawa, T.; Suzuki, M. Oxidation Reactivity of Bis(mu-oxo) Dinickel(III) Complexes: Arene Hydroxylation of the Supporting Ligand. *Angew. Chem., Int. Ed.* **2009**, *48*, 3304−3307.
(58) Speight, J. G. *Handbook of Industrial Hydrocarbon Processes*; Elsevier Inc.: Burlington, MA, 2011.
(59) Lunsford, J. H. The Catalytic Oxidative Coupling of Methane. *Angew. Chem., Int. Ed.* **1995**, *34*, 970−980.
(60) Mleczko, L.; Baerns, M. Catalytic Oxidative Coupling of Methane - Reaction-Engineering Aspects and Process Schemes. *Fuel Process. Technol.* **1995**, *42*, 217−248.

dx.doi.org/10.1021/la501184b | *Langmuir* 2014, 30, 8558−8569